Universal density shift coefficients for the thermal conductivity and shear viscosity of a unitary Fermi gas

Xiang Li[®], J. Huang[®], and J. E. Thomas[®]*

Department of Physics, North Carolina State University, Raleigh, North Carolina 27695, USA



(Received 21 February 2024; revised 11 June 2024; accepted 4 October 2024; published 23 October 2024)

We measure universal temperature-independent density shifts for the thermal conductivity κ_T and shear viscosity η , relative to the high temperature limits, for a normal phase unitary Fermi gas confined in a box potential. We show that a time-dependent kinetic theory model enables extraction of the hydrodynamic transport times τ_{η} and τ_{κ} from the time-dependent free decay of a spatially periodic density perturbation, yielding the static transport properties and density shifts, corrected for finite relaxation times.

DOI: 10.1103/PhysRevResearch.6.L042021

Measurements of the universal hydrodynamic transport properties of a unitary Fermi gas connect ultracold atoms to nuclear matter [1–3] and provide new challenges to theoretical predictions [4–15]. A unitary Fermi gas is a strongly interacting, scale-invariant, quantum many-body system, created by tuning a trapped, two-component cloud near a collisional (Feshbach) resonance [16]. At resonance, the thermodynamic and transport properties are universal functions of the density and temperature [17], permitting parameter-free comparisons with predictions. Early measurements on expanding Fermi gas clouds with nonuniform density [18,19] have made way for new measurements in optical box potentials [20], where the density is nearly uniform [21–26]. For a unitary Fermi gas, the second bulk viscosity vanishes, as predicted for scale-invariant systems [27,28] and demonstrated in experiments on conformal symmetry [29]. Hence, in the normal phase at temperatures above the superfluid transition [30], the hydrodynamic transport properties comprise only the shear viscosity η and the thermal conductivity κ_T .

Remarkably, the measured shear viscosity and thermal conductivity in the normal phase appear to be fit by the simple expressions [12,23,31],

$$\eta = \frac{15}{32\sqrt{\pi}} \frac{(mk_B T)^{3/2}}{\hbar^2} + \alpha_{2\eta} \, \hbar n_0, \tag{1}$$

and

$$\kappa_T = \frac{15}{4} \frac{k_B}{m} \, \eta(\alpha_{2\eta} \to \alpha_{2\kappa}) \tag{2}$$

with k_B the Boltzmann constant and m the atom mass. The density shift coefficients $\alpha_{2\eta}$ and $\alpha_{2\kappa}$ are temperature-independent fit parameters. Here, the temperature T and

Published by the American Physical Society under the terms of the Creative Commons Attribution 4.0 International license. Further distribution of this work must maintain attribution to the author(s) and the published article's title, journal citation, and DOI.

density n_0 contributions can be understood by dimensional analysis. For the shear viscosity, with a dimension of momentum/area, we expect $\eta \propto \hbar/L^3$, with L a length scale. At high temperature, $L \rightarrow \lambda_T$, the thermal de Broglie wavelength $\propto T^{-1/2}$. At lower temperature, where the cloud is degenerate, $1/L^3 = n_0$. For both η and κ_T , the leading high temperature $T^{3/2}$ dependence has been obtained by variational calculations for a unitary gas in the two-body Boltzmann limit [4,6,12]. In contrast to the two-body $T^{3/2}$ coefficients, the density shift coefficients $\alpha_{2\eta}$ and $\alpha_{2\kappa}$ are unknown universal many-body parameters, which can arise in Fermi gases by Pauli blocking. In calculations of the transport times for a unitary Fermi gas, however, it has been noted that Pauli blocking appears to be nearly canceled by in-medium scattering [13]. Precise measurements of the density shifts therefore test the degree of this fundamental cancellation.

In this work, we measure the universal temperatureindependent density shifts for the static shear viscosity and thermal conductivity of a normal phase unitary Fermi gas, confined in a uniform box potential. The time-dependent freedecay of an initial spatially periodic density perturbation is observed and analyzed using a time-dependent kinetic theory model to move beyond the fast-relaxation approximation, assumed for extracting transport properties in previous experiments [22–24]. The model corrects for the suppression of each transport property measured at finite frequency ω , relative to the static value [32]. We use this model to extract the universal hydrodynamic transport times τ_n and τ_κ from the data. The model is examined by measurements for several different perturbation wavelengths λ , which alters the frequency $\propto 1/\lambda$ and the damping rates $\propto 1/\lambda^2$. The extracted relaxation times determine the static shear viscosity and thermal conductivity, yielding the two universal density shift parameters $\alpha_{2\eta}$, $\alpha_{2\kappa}$, corrected for the finite response time over which the viscous force and heat current relax to their Navier-Stokes forms.

The experiments employ ultracold $^6\mathrm{Li}$ atoms in a balanced mixture of the two lowest hyperfine states, which are evaporatively cooled in a CO_2 laser trap and loaded into a box potential, Fig. 1, producing a sample of nearly uniform density n_0 . The box comprises six sheets of blue-detuned light,

^{*}Contact author: jethoma7@ncsu.edu

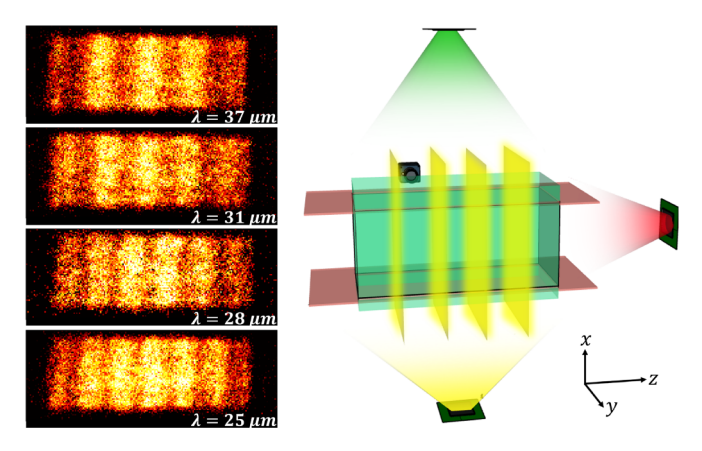


FIG. 1. A unitary Fermi gas is loaded into a repulsive box potential created by two digital micromirror devices DMDs (top, right). A third DMD (bottom) generates a static spatially periodic perturbation $\delta U(z)$ with an adjustable wavelength λ , creating spatially periodic initial 1D density profiles (left). After δU is abruptly extinguished, the dominant Fourier component exhibits an oscillatory decay (see Fig. 2).

created by two digital micromirror devices (DMDs) [21,23] (top and right). The box potential $U_0(\mathbf{r})$ yields a rectangular density profile with typical dimensions $(x, y, z) = (52 \times 50 \times 175) \, \mu \text{m}$. The density varies slowly in the direction of the long (z) axis, due to the harmonic confining potential $\propto z^2$ arising from the curvature of the bias magnetic field, which has little effect on the shorter x and y axes. The typical total central density is $n_0 = 3.3 \times 10^{11} \, \text{atoms/cm}^3$, with the Fermi energy $\epsilon_F \equiv k_B T_F = k_B \times 0.18 \, \mu \text{K}$ and Fermi speed $v_F \simeq 2.25 \, \text{cm/s}$. The box depth $U_0 \simeq 0.75 \, \mu \text{K}$ (see Ref. [23]).

We employ an optical system with a third DMD, Fig. 1 (bottom), to independently project a static optical potential $\delta U(z)$, which is spatially periodic along one axis z with an adjustable wavelength λ . This creates an initial density perturbation $\delta n(z)/n_0 = A \sin(2\pi z/\lambda)$, where a small A = 10%is chosen for measurement in the hydrodynamic linear response regime [31]. The third DMD is illuminated with a low intensity beam to utilize its full dynamic range. Once equilibrium is established, the perturbing potential is abruptly extinguished, causing an oscillatory decay of the measured density perturbation $\delta n(z, t) = n(z, t) - n_0(z)$, with n(z, t) the doubly integrated 3D density. By performing a fast Fourier transform (FFT) of $\delta n(z, t)$ at each time, in a region containing an integer number (typically 3–4) of spatial periods, we obtain $\delta n(q, t)$, Fig. 2. As shown previously [23], in a fast-relaxation approximation, $\delta n(q, t)$ contains a thermally diffusive mode $(\simeq 35\%)$ that decays at a rate $\propto \kappa_T$ and an oscillating first sound mode, which decays at a rate dependent on both η and κ_T , yielding η and κ_T , albeit uncorrected for the finite transport times.

To include the finite response times, we derive a relaxation model in the linear response regime by constructing four coupled equations: two describe the changes in the density $\delta n(z,t)$ and temperature $\delta T(z,t)$, and two describe the relaxation of the viscous force and heat current [6,7]. We ignore the box potential, since we measure the free-decay over time scales that avoid perturbing $\delta n(z,t)$ in the measured central

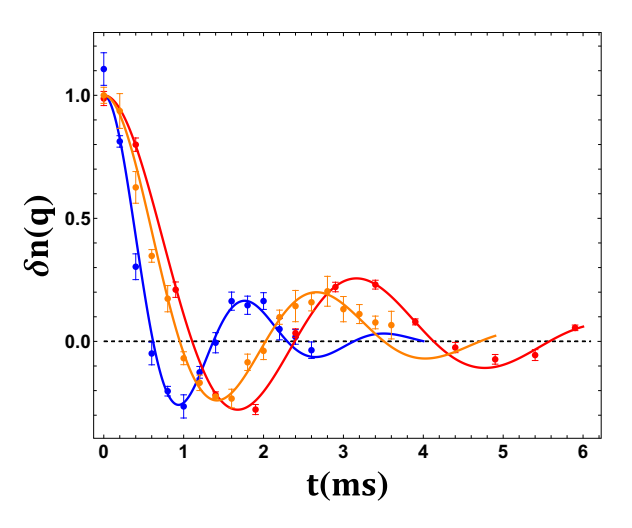


FIG. 2. Fourier component of the density perturbation $\delta n(q,t)$ with $q=2\pi/\lambda$, for wavelengths $\lambda=40.0\,\mu\text{m}$, 31.3 μm , and 22.7 μm (red, orange, and blue) at reduced temperatures $T/T_F=0.42,\,0.36$, and 0.32, respectively. Dots: data; Curves: hydrodynamic relaxation time model. The error bars are the standard deviation of the mean of $\delta n(q,t)$ for 5–8 runs, taken in random time order.

region by reflections from the boundaries. After the perturbing potential is extinguished, the density change obeys [31]

$$\delta \ddot{n} = c_T^2 \, \partial_z^2 (\delta n + \delta \tilde{T}) + \delta Q_n. \tag{3}$$

The c_T^2 term in Eq. (3) arises from the pressure change with c_T the isothermal sound speed, and

$$\delta \dot{Q}_{\eta} + \frac{1}{\tau_{\eta}} \delta Q_{\eta} = \frac{4}{3} \frac{p}{mn_0} \partial_z^2 \delta \dot{n}$$
 (4)

describes the relaxation of the viscous damping force [31]. Here the pressure $p = \frac{2}{5}n\epsilon_F f_E(\theta)$, where the universal function $f_E(\theta)$ has been measured [30], n_0 is the background density, and we have used the continuity equation to eliminate the velocity field. For fast relaxation, Eq. (4) yields the usual Navier-Stokes form for δQ_{η} in Eq. (3) with $\eta = \tau_{\eta} p$ the static shear viscosity, independent of the single particle phase space distribution [31].

In Eq. (3), we have defined a scaled temperature, $\delta \tilde{T} = n_0 \beta \, \delta T$ with a dimension of density, where $\beta = -1/n(\partial n/\partial T)_P$ is the thermal expansivity [31]. We find

$$\delta \dot{\tilde{T}} = \epsilon_{LP} \, \delta \dot{n} + \delta Q_{\kappa}. \tag{5}$$

The Landau-Placzek parameter $\epsilon_{LP} \equiv c_{P_1}/c_{V_1} - 1$ determines the adiabatic change in the temperature arising from the change in density. The heat capacities per particle at constant volume c_{V_1} and at constant pressure c_{P_1} are determined by the measured equation of state $f_E(\theta)$ [30,31], and the heat current obeys

$$\delta \dot{Q}_{\kappa} + \frac{1}{\tau_{\kappa}} \delta Q_{\kappa} = \frac{5}{2} \frac{k_B}{m} \frac{p}{n_0 c_{V_1}} \partial_z^2 \delta \tilde{T}. \tag{6}$$

For fast relaxation, Eq. (6) yields the usual heating rate δQ_{κ} in Eq. (5) with $\kappa_T = \frac{5}{2} \frac{k_B}{m} \tau_{\kappa} p$ the static thermal conductivity. Here, the factor 5/2 is dependent on a Maxwell-Boltzmann approximation for the single particle phase space distribution [31].

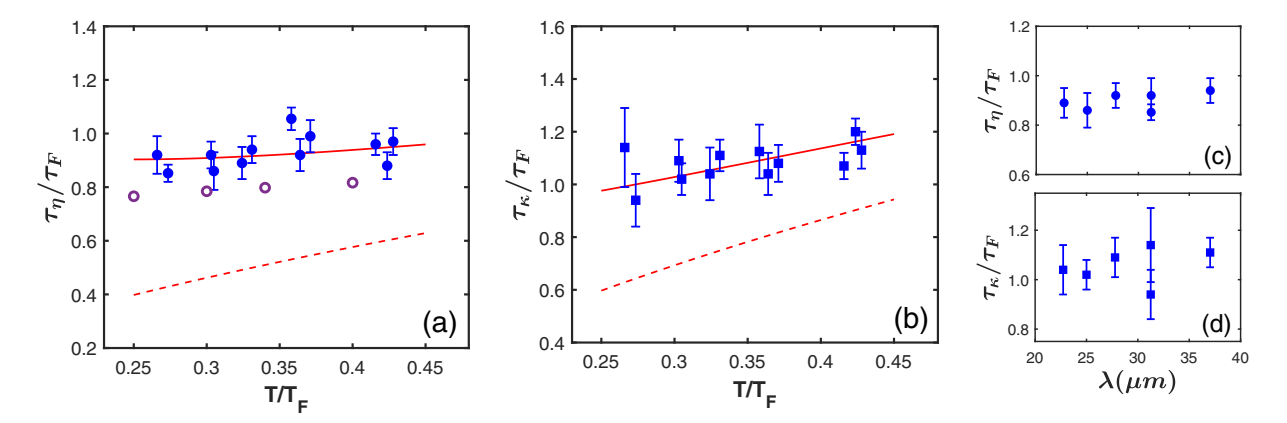


FIG. 3. Hydrodynamic relaxation times in units of the Fermi time $\tau_F \equiv \lambda_F/v_F = \pi \hbar/\epsilon_F$ versus reduced temperature T/T_F .(a) τ_η for the shear viscosity (solid blue circles). Open circles are predictions of Ref. [8], Fig. 6 divided by π [33]. (b) τ_κ for the thermal conductivity (blue squares). Red curves show fits with the density shift coefficients $\alpha_{2\eta} = 0.45$ and $\alpha_{2\kappa} = 0.22$, which are the same as obtained from the fits to Figs. 4(a) and 4(b). Red dashed curves: High temperature limits, where $\alpha_{2\eta} = 0$ and $\alpha_{2\kappa} = 0$ and $\tau_\kappa/\tau_\eta = 3/2$. [(c), (d)] Wavelength dependence for $T/T_F \simeq 0.30$. Error bars are statistical [34].

A spatial Fourier transform of Eqs. (3)-(6) yields coupled linear equations for $\delta \ddot{n}(q,t)$, $\delta \tilde{T}(q,t)$, $\delta \dot{Q}_{n}(q,t)$, and $\delta \dot{Q}_{\kappa}(q,t)$ with $q=2\pi/\lambda$. As the system is initially in mechanical equilibrium and isothermal, only $\delta n(q, 0) \equiv A \neq 0$. Formally, the exact solutions contain four modes [31]. However, the contributions of the two fast modes to $\delta n(q, t)$ are small ($\simeq 1$ %) [31] and decay quickly, since τ_n and $\tau_{\kappa} \simeq$ 100 µs in our experiments, so they are not directly measured. The remaining thermally diffusive mode and first sound mode then dominate. The free decay of $\delta n(q, t)$ is fit by the model using the amplitude A, the frequency $c_T q$, and the transport relaxation times τ_{η} , τ_{κ} as fit parameters, instead of A, $c_T q$, η , and κ_T [23]. The wavelength of the perturbation and the fit frequency $c_T q$ self-consistently determine the sound speed c_T and the corresponding reduced temperature $T/T_F = \theta(c_T/v_F)$ from $f_E(\theta)$, with the Fermi speed v_F given for the average central density n_0 [31]. Figure 2 shows fits of the relaxation model (solid curves) to typical data ($\times 1/A$).

Our fitted transport times τ_{η} for the shear viscosity and τ_{κ} for the thermal conductivity are shown as functions of

 $\theta = T/T_F$ in Fig. 3. The transport times are given in units of the Fermi time $\tau_F \equiv \lambda_F/v_F = \pi \hbar/\epsilon_F \simeq 120 \,\mu s$. We see that the fitted τ_η is in reasonable agreement with the predictions of Ref. [8], Fig. 6 [33]. The wavelength dependence of τ_η and τ_κ is shown for $\theta \simeq 0.30$, demonstrating negligible λ dependence.

The fitted τ_{η} determines the static shear viscosity $\eta = \tau_{\eta} p$ shown in Fig. 4(a) (blue circles), which is in reasonable agreement with predictions of Ref. [8], Fig. 7 (Open circles). Equation (1), in units of $\hbar n_0$, gives

$$\eta(\theta) = \alpha_{3/2} \, \theta^{3/2} + \alpha_{2\eta},\tag{7}$$

where $\alpha_{3/2} = \frac{45\pi^{3/2}}{64\sqrt{2}} \simeq 2.77$ [4,6,12]. The red curve in Fig. 4(a) shows the fit for $\eta(\theta)$ with the density shift coefficient $\alpha_{2\eta}$ as the only fit parameter, yielding $\alpha_{2\eta} = 0.45(04)$. The red -dashed curve in Fig. 4(a) is the high temperature limit, $\alpha_{2\eta} = 0$. The red curve in Fig. 3(a) shows the fit for $\tau_{\eta} = \eta/p$, with $p = \frac{2}{5}n\epsilon_F f_E(\theta)$, yielding $\alpha_{2\eta} = 0.45$, the same as obtained from the fit to Fig. 4(a).

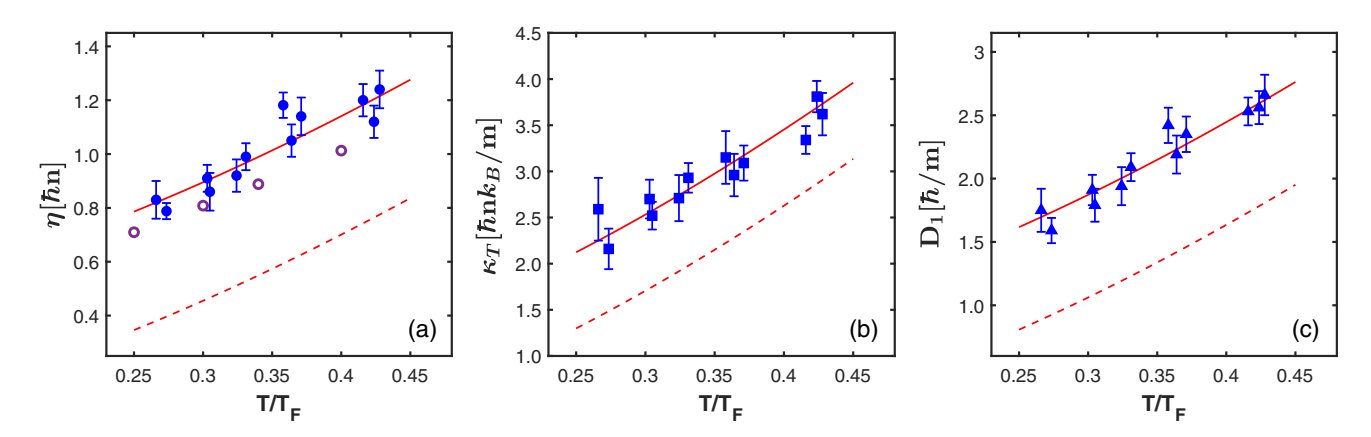


FIG. 4. Transport properties obtained from the measured transport times τ_{η} and τ_{κ} versus reduced temperature $\theta = T/T_F$. (a) Shear viscosity (blue circles). Open circles are predictions of Ref. [8], Fig. 7. (b) Thermal conductivity (blue squares). (c) First sound diffusivity (blue Triangles). Red solid curves include the density shift coefficients $\alpha_{2\eta} = 0.45$ in Eq. (7) and $\alpha_{2\kappa} = 0.22$ in Eq. (8). Red dashed curves are the high temperature limits, where $\alpha_{2\eta} = 0$ and $\alpha_{2\kappa} = 0$. Error bars are statistical.

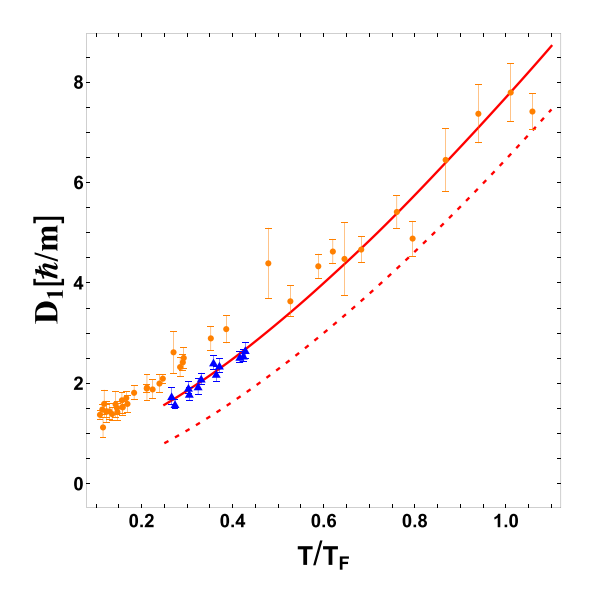


FIG. 5. Sound diffusivity in units of \hbar/m versus reduced temperature $\theta = T/T_F$. Blue triangles: D_1 of Fig. 4(c). Orange dots: Sound diffusivity data from sound attenuation [22]. Red solid curve from Fig. 4(c): $D_1[\hbar/m] = \frac{4}{3} (2.77 \, \theta^{3/2} + 0.45) + \frac{5}{2} \frac{\theta}{f_E(\theta)} (2.77 \, \theta^{3/2} + 0.22)$. Red dashed curve (high temperature limit) $D_1[\hbar/m] = 7/3 \times 2.77 \, \theta^{3/2}$.

Similarly, the fitted τ_{κ} determines the static thermal conductivity $\kappa_T = \frac{5}{2} \frac{k_B}{m} \tau_{\kappa} p$ shown in Fig. 4(b) (blue squares). In the high temperature two-body Boltzmann limit, one can show that $\tau_{\kappa}/\tau_{\eta} = 3/2$ for any isotropic collision cross section $d\sigma/d\Omega$, so that $\kappa_T = \frac{15}{4} \frac{k_B}{m} \eta$. Equation (2), in units of $n_0 \hbar k_B/m$, gives

$$\kappa_T(\theta) = \frac{15}{4} \left(\alpha_{3/2} \, \theta^{3/2} + \alpha_{2\kappa} \right).$$
(8)

The red curve in Fig. 4(b) shows the fit of $\kappa_T(\theta)$ with the density shift coefficient $\alpha_{2\kappa}$ as the only fit parameter, yielding $\alpha_{2\kappa} = 0.22(03)$, i.e., the shift is $15/4 \times 0.22$ in units of $n_0 \hbar k_B/m$. The red dashed curve in Fig. 4(b) is the high temperature limit, $\alpha_{2\kappa} = 0$. The red curve in Fig. 3(b) shows the fit for $\tau_{\kappa} = \frac{2}{5} \frac{m}{k_B} \kappa_T/p$, yielding $\alpha_{2\kappa} = 0.22$, the same as obtained from the fit to Fig. 4(b). We find that the measured κ_T are significantly smaller than predicted in [13] and larger than predicted in [15].

Finally, Fig. 4(c) shows the corresponding first sound diffusivity [31,35] D_1 in units of \hbar/m . The fitted transport

times determine $D_1[\hbar/m] = \frac{8\pi}{15} \frac{\tau_n}{\tau_F} f_E(\theta) + \frac{2\pi}{3} \frac{\tau_k}{\tau_F} \theta$ (blue triangles). The red solid curve gives D_1 in terms of the fits of Figs. 4(a) and 4(b) for the static shear viscosity and thermal conductivity, $D_1 = 4/3 (2.77 \, \theta^{3/2} + 0.45) + (n \, k_B T/p) (2.77 \, \theta^{3/2} + 0.22)$. Here, $n \, k_B T/p = 5/2 \, \theta/f_E(\theta)$ for the unitary gas, where p is the pressure [31]. The red dashed curve is the high temperature limit $D_1 = 7/3 \times 2.77 \, \theta^{3/2}$.

The fitted density shift coefficients for the shear viscosity and thermal conductivity are expected to be independent of reduced temperature. In Fig. 5, we compare our measurements and predictions based on our measurements (red solid curve) to the first sound diffusivity measured over a wider range of reduced temperatures by sound attenuation [22]. We see that the red solid curve from Fig. 4(c) is in agreement with sound attenuation data for $T/T_F > 0.5$. However, the sound attenuation data exhibit a nearly constant upward shift relative to our hydrodynamic relaxation data where $T/T_F < 0.5$, which is not yet understood.

In conclusion, we have shown that time-domain hydrodynamic relaxation experiments are well-suited for timedependent kinetic theory models that explicitly include the transport times to determine the static transport properties. We find that the fitted transport times for the thermal current and viscous force vary slowly for reduced temperatures $0.25 \le T/T_F \le 0.45$ and are close to one Fermi time λ_F/v_F , small, but not negligible, compared to the time scales for the oscillatory decay of the density perturbation. We obtain a ratio $\tau_{\kappa}/\tau_{\eta} \simeq 1.2$ at $T/T_F = 0.4$, significantly below the high temperature Boltzmann limit, $\tau_{\kappa}/\tau_{\eta} = 3/2$ [13]. The transport times determine the universal temperature-independent density shifts, providing a single parameter test of predictions for each of the static transport properties. Our measurements emphasize the need for new calculations of the leading density-dependent corrections to the hydrodynamic transport properties as well as more sophisticated time-dependent relaxation models.

We thank Thomas Schäfer for stimulating discussions, Ilya Arakelyan for help with the optical system, Parth Patel and Martin Zwierlein for providing their sound diffusivity data, and Tilman Enss for providing predictions of the viscosity and corresponding transport time. Primary support for this research is provided by the National Science Foundation (PHY-2006234 and PHY-2307107). Additional support is provided by the Air Force Office of Scientific Research (FA9550-22-1-0329).

^[1] A. Adams, L. D. Carr, T. Schäfer, P. Steinberg, and J. E. Thomas, Strongly correlated quantum fluids: Ultracold quantum gases, quantum chromodynamic plasmas and holographic duality, New J. Phys. 14, 115009 (2012).

^[2] I. Bloch, J. Dalibard, and S. Nascimbène, Quantum simulations with ultracold quantum gases, Nat. Phys. **8**, 267 (2012).

^[3] G. C. Strinati, P. Pieri, G. Röpke, P. Schuck, and M. Urban, The BCS-BEC crossover: From ultra-cold Fermi gases to nuclear systems, Phys. Rep. 738, 1 (2018).

^[4] G. M. Bruun and H. Smith, Shear viscosity and damping for a Fermi gas in the unitary limit, Phys. Rev. A **75**, 043612 (2007).

^[5] E. Taylor and M. Randeria, Viscosity of strongly interacting quantum fluids: Spectral functions and sum rules, Phys. Rev. A 81, 053610 (2010).

^[6] M. Braby, J. Chao, and T. Schäfer, Thermal conductivity and sound attenuation in dilute atomic Fermi gases, Phys. Rev. A 82, 033619 (2010).

- [7] M. Braby, J. Chao, and T. Schäfer, Viscosity spectral functions of the dilute Fermi gas in kinetic theory, New J. Phys. 13, 035014 (2011).
- [8] T. Enss, R. Haussmann, and W. Zwerger, Viscosity and scale invariance in the unitary Fermi gas, Ann. Phys. **326**, 770 (2011).
- [9] H. Guo, D. Wulin, C.-C. Chien, and K. Levin, Microscopic approach to shear viscosities of unitary Fermi gases above and below the superfluid transition, Phys. Rev. Lett. 107, 020403 (2011).
- [10] G. Wlazłowski, P. Magierski, and J. E. Drut, Shear viscosity of a unitary Fermi gas, Phys. Rev. Lett. 109, 020406 (2012).
- [11] P. Romatschke and R. E. Young, Implications of hydrodynamic fluctuations for the minimum shear viscosity of the dilute Fermi gas at unitarity, Phys. Rev. A **87**, 053606 (2013).
- [12] M. Bluhm, J. Hou, and T. Schäfer, Determination of the density and temperature dependence of the shear viscosity of a unitary Fermi gas based on hydrodynamic flow, Phys. Rev. Lett. 119, 065302 (2017).
- [13] B. Frank, W. Zwerger, and T. Enss, Quantum critical thermal transport in the unitary Fermi gas, Phys. Rev. Res. 2, 023301 (2020).
- [14] J. Hofmann, High-temperature expansion of the viscosity in interacting quantum gases, Phys. Rev. A 101, 013620 (2020).
- [15] H. Zhou and Y. Ma, Thermal conductivity of an ultracold Fermi gas in the BCS-BEC crossover, Sci. Rep. 11, 1228 (2021).
- [16] K. M. O'Hara, S. L. Hemmer, M. E. Gehm, S. R. Granade, and J. E. Thomas, Observation of a strongly interacting degenerate Fermi gas of atoms, Science 298, 2179 (2002).
- [17] T.-L. Ho, Universal thermodynamics of degenerate quantum gases in the unitarity limit, Phys. Rev. Lett. 92, 090402 (2004).
- [18] C. Cao, E. Elliott, J. Joseph, H. Wu, J. Petricka, T. Schäfer, and J. E. Thomas, Universal quantum viscosity in a unitary Fermi gas, Science **331**, 58 (2011).
- [19] J. A. Joseph, E. Elliott, and J. E. Thomas, Shear viscosity of a unitary Fermi gas near the superfluid phase transition, Phys. Rev. Lett. **115**, 020401 (2015).
- [20] N. Navon, R. P. Smith, and Z. Hadzibabic, Quantum gases in optical boxes, Nat. Phys. 17, 1334 (2021).
- [21] L. Baird, X. Wang, S. Roof, and J. E. Thomas, Measuring the hydrodynamic linear response of a unitary Fermi gas, Phys. Rev. Lett. 123, 160402 (2019).

- [22] P. B. Patel, Z. Yan, B. Mukherjee, R. J. Fletcher, J. Struck, and M. W. Zwierlein, Universal sound diffusion in a strongly interacting Fermi gas, Science **370**, 1222 (2020).
- [23] X. Wang, X. Li, I. Arakelyan, and J. E. Thomas, Hydrodynamic relaxation in a strongly interacting Fermi gas, Phys. Rev. Lett. 128, 090402 (2022).
- [24] X. Li, X. Luo, S. Wang, K. Xie, X.-P. Liu, H. Hu, Y.-A. Chen, X.-C. Yao, and J.-W. Pan, Second sound attenuation near quantum criticality, Science 375, 528 (2022).
- [25] H. Hu, P. Zou, and X.-J. Liu, Low-momentum dynamic structure factor of a strongly interacting Fermi gas at finite temperature: A two-fluid hydrodynamic description, Phys. Rev. A 97, 023615 (2018).
- [26] Z. Yan, P. B. Patel, B. Mukherjee, C. J. Vale, R. J. Fletcher, and M. W. Zwierlein, Thermography of the superfluid transition in a strongly interacting Fermi gas, Science 383, 629 (2024).
- [27] D. T. Son, Vanishing bulk viscosities and conformal invariance of the unitary Fermi gas, Phys. Rev. Lett. 98, 020604 (2007).
- [28] Y.-H. Hou, L. P. Pitaevskii, and S. Stringari, Scaling solutions of the two-fluid hydrodynamic equations in a harmonically trapped gas at unitarity, Phys. Rev. A 87, 033620 (2013).
- [29] E. Elliott, J. A. Joseph, and J. E. Thomas, Observation of conformal symmetry breaking and scale invariance in expanding Fermi gases, Phys. Rev. Lett. **112**, 040405 (2014).
- [30] M. Ku, A. T. Sommer, L. W. Cheuk, and M. W. Zwierlein, Revealing the superfluid lambda transition in the universal thermodynamics of a unitary Fermi gas, Science 335, 563 (2012).
- [31] See Supplemental Material at http://link.aps.org/supplemental/ 10.1103/PhysRevResearch.6.L042021 for discussion of the linearized hydrodynamic equations, the kinetic theory relaxation model, and the determination of the static transport properties.
- [32] In a simple Drude model with a transport time τ , the electrical conductivity is $\sigma(\omega) = \sigma(0)/(1 i\omega\tau)$.
- [33] Note that the Fermi time defined in Ref. [8], Fig. 6 is \hbar/ϵ_F , which is a factor of π smaller than λ_F/v_F .
- [34] The vertical error bars in Figs. 3 and 4 denote $\pm \sqrt{2\epsilon_{ii}}$, where ϵ_{ij} is the error matrix obtained from $\chi^2(\tau_{\eta}, \tau_{\kappa})$ with A and c_T fixed.
- [35] L. D. Landau and E. M. Lifshitz, Fluid Dynamics, Course of Theoretical Physics Vol. VI (Pergamon Press, Oxford, 1959)